



Ultrathin δ -MnO₂ nanoribbons for highly efficient removal of a human-related low threshold odorant - acetic acid

Tongzhou Xu^a, Pengyi Zhang^{a,b,*}, Huiyu Zhang^a

^a State Key Joint Laboratory of Environment Simulation and Pollution Control, School of Environment, Tsinghua University, Beijing 100084, China

^b Beijing Key Laboratory for Indoor Air Quality Evaluation and Control, Beijing 100084, China

ARTICLE INFO

Keywords:

δ -MnO₂
Catalytic removal
Human-emitted VOCs
Indoor air
Ventilation

ABSTRACT

Efficient removal of human-emitted gaseous pollutants in indoor air may greatly reduce ventilation-related energy consumption, however few efforts have been made. Here we reported the room and low-temperature catalytic removal of a human-emitted odorant - acetic acid with odor threshold of 5.6 ppb. Ultrathin δ -MnO₂ nanoribbons (δ -MnO₂ UTNRs) with the thickness of 1–1.5 nm and aspect ratio of 200–600 was synthesized, which produced abundant active oxygen species such as hydroxyl radicals and superoxide at room temperature without light irradiation. Accordingly, as-prepared δ -MnO₂ UTNRs could transform acetic acid into CO₂ even at room temperature. The 100% one-through removal capacity for ~1 ppm acetic acid was about 20 mg/g, and it could be completely regenerated at 140 °C. This study opens a new research direction and demonstrates that it is possible to catalytically remove human-emitted gaseous pollutant at low and even at room temperature.

1. Introduction

In recent years, the health problems caused by poor indoor air quality have aroused widespread concern [1,2]. Volatile organic compounds (VOCs) are the main gaseous pollutants in indoor air [3–5]. Exposure to VOCs has been associated with many acute and chronic diseases, and even cancers [6]. Previous studies often focused on a small subset of VOCs released by building decoration materials that are known to cause adverse health effects, such as formaldehyde, benzene, toluene, ethylacetate, *n*-hexane and so on [7–12]. However, few attentions have been paid to the human-related VOCs especially those with pungent odor. People exhale many kinds of pollutants such as CO₂ and various VOCs, and these human-related bio-effluents normally diluted and exchanged outdoors by ventilation. And nearly 30% of energy delivered to buildings is dissipated in the air that leaves buildings through ventilation and exfiltration [13]. Buildings is the fourth greenhouse gas emission department ranked after power, industry and transport [14]. It is therefore an important and interesting research field to remove human-related bio-effluents by catalysis or adsorption rather than ventilation, which is of great significance to reduce building's energy consumption and greenhouse gas emission.

Due to its high production rate by human and convenient measurement, CO₂ has been widely used as an indicator of the required outdoor

fresh air. And the indoor CO₂ level \leq 1000 ppm is generally required, and the corresponding fresh air is about 25–30 m³/h per capita, which will cost a lot of energy. However, no statistically significant effects on perceived air quality, acute health symptoms, or cognitive performance were seen when humans exposed to 3000 ppm CO₂ which was extra added [15]. Thus, it is other bio-effluents not CO₂ bring negative impacts on human health. Acetic acid is a typical odorant with high human emission rate and very low odor threshold (~5.6 ppb), which will deteriorate indoor air quality and affect human health [16–18]. It was found that in a well-ventilated classroom, human-emitted VOCs were the dominant pollution source, and the human-related acetic acid emission rate was as high as 329 μ g/h/person ranked the third VOC emitted by humans [16]. Thus, here we selected acetic acid as a representative bio-effluent to explore feasible treatment method.

In the past decade, supported noble metal (e.g. Pt/TiO₂) and MnO₂ have been demonstrated to show efficient room-temperature catalytic activity for formaldehyde (HCHO), which is the best known indoor air pollutant [19,20]. However, except HCHO, the room-temperature catalytic removal of other indoor organic pollutants has rarely investigated. MnO₂ is an environmentally friendly transition metal oxide with a variety of crystal structures. In recent years, it has been found that birnessite-type MnO₂ (δ -MnO₂) exhibits significant room or low-temperature catalytic activity for HCHO [20], ozone [21,22] and

* Correspondence to: School of Environment, Tsinghua University, Beijing 100084, China.

E-mail address: zpy@tsinghua.edu.cn (P. Zhang).

<https://doi.org/10.1016/j.apcatb.2022.121273>

Received 12 November 2021; Received in revised form 25 February 2022; Accepted 28 February 2022

Available online 2 March 2022

0926-3373/© 2022 Elsevier B.V. All rights reserved.

VOCs [23]. For example, Zhang *et al.* [24] found that δ -MnO₂ has the highest catalytic activity for HCHO removal among the four crystal forms of MnO₂ (α -, β -, γ - and δ -MnO₂), which is attributed to its layer structure and abundant active oxygen species. Selvakumar *et al.* [25] found that δ -MnO₂ has excellent selective conversion of HCHO to CO₂, and formate ions interact with manganese and potassium ions while carbonate ions interact only with potassium ions by using time-of-flight secondary ion mass spectroscopy. Rong *et al.* [26] reported that ultrathin δ -MnO₂ nanosheets showed high activity for HCHO removal at room temperature. Cao *et al.* [27] reported that ammonium ions (NH₄⁺)-modulated ultrathin δ -MnO₂ nanosheets exhibited great activity for ozone decomposition at 25 °C. Zhang *et al.* reported that atomically dispersed noble metal (Pt) or rare earth metal (Y or La) on δ -MnO₂ significantly enhanced the catalytic decomposition of toluene [9,28]. It is well-known that the crystal structures as well as morphologies may greatly influence their catalytic activity. Though various morphologies of δ -MnO₂ such as nanosheet, nanosphere, nanoplate and nanorod have been reported in the literature [29–31], to the best of our knowledge, the synthesis of the δ -MnO₂ nanoribbons with few layers has not been reported. Herein, the ultrathin (thickness of 1–1.5 nm) δ -MnO₂ nanoribbons (hereafter referred as δ -MnO₂ UTNRs) with the width of 5–10 nm and the length of 1–3 μ m were synthesized and self-assembled without the cover of any surfactants or organic stabilizers, which will greatly impede the catalytic process. As-synthesized δ -MnO₂ UTNRs exhibited excellent adsorption capacity and catalytic activity in transforming acetic acid into CO₂ at room temperature in the presence of water vapor.

2. Experimental section

2.1. Catalyst preparation

All the chemicals are analytical grade and used without further purification. The δ -MnO₂ UTNRs was synthesized by a facile redox between KMnO₄ and ethylene glycol (EG) with the assistance of oleylamine (OAm). First, 2.42 g KMnO₄ was added into 35 mL deionized water with stirring to dissolve completely. 0.45 mL oleylamine, 0.15 mL ethylene glycol and 15 mL deionized water were mixed together with ultrasonication for 10 min to form emulsion. Then, the KMnO₄ solution was directly added to the continuously stirred emulsion. The mixed solution in a sealed bottle was transferred to the 80 °C water bath with continuously stirring. After 2 h, 0.5 mL H₂SO₄ aqueous solution (5 mmol H⁺) was added to the mixed solution, which help to volatilize some of carbonate (generated from the reaction between KMnO₄ and ethylene glycol) into CO₂ and provide an appropriate pH condition for the formation of MnO₂ nanoribbon via the edge-to-edge oriented attachment of primary fine MnO₂ nanosheets. After another 2 h, the solid precipitate was filtered, washed several times with cyclohexane, ethanol, and deionized water to remove the residual organics, and dried in air at 105 °C for 12 h, finally the δ -MnO₂ UTNRs was obtained. For comparison, the sample without addition of H₂SO₄ aqueous solution or added at the starting time (0 h) were also synthesized. These two samples and that with addition of H₂SO₄ after 2 h were named as MnO₂-NH, MnO₂-OH and MnO₂-2H, respectively.

2.2. Characterization

X-ray powder diffraction (XRD) patterns of samples were performed from Rigaku D/max-RB (Bruker, Germany) with Cu-K α (λ = 0.15418 nm) radiation operated at 40 kV and 100 mA. The size and morphology of as-prepared samples were characterized by using a Hitachi S-5500 field-emission scanning electron microscope (FESEM, Hitachi, Japan) with an accelerating voltage of 5.0 kV. The high-resolution transmission electron microscopy (HRTEM) images were characterized by using a JEM-2011F electron microscope (JEOL, Japan) at a voltage of 200 kV. The thickness of samples was acquired by atomic force microscopy

(AFM) in tapping mode with a Bruker Dimension ICON. Surface functional groups were performed by a Thermo Fisher Fourier transform infrared spectrometer (FTIR, Nexus-870, USA). The total organic carbon (TOC) of samples were detected by Total Organic Carbon Analyzer with SSM-5000A solid sample module (Shimadzu, Japan). The Micromeritics ASAP2020 nitrogen adsorption apparatus (USA) was used to measure the surface area of samples at – 196 °C. X-ray photoelectron spectroscopy (XPS) was measured by an ESCALAB 250Xi apparatus with Al-K α radiation (Thermo Fisher, USA) to acquire the binding energies and valence states of Mn and O elements. Binding energies were calibrated using the energy of the C 1s peak at 284.8 eV, and the spectral resolution was 0.05 eV. Raman spectra were detected by the confocal Raman microscopes (Renishaw, inVia) with a laser source of 532 nm. Electronic spinning resonance (ESR) spectra of samples were obtained by Bruker EPR 300E spectrometer using 5, 5-dimethyl-1-pyrroline N-oxide (DMPO) as trapping agent in water and dimethyl sulfoxide (DMSO) at 25 °C.

The H₂ temperature programmed reduction (H₂-TPR) and O₂ temperature programmed desorption (O₂-TPD) profiles were obtained in a Micromeritics AutoChem II 2920 instrument equipped with a thermal conductivity detector (TCD). For the H₂-TPR process, 50 mg sample in a quartz reactor was heated to 105 °C in He gas (50 mL·min^{–1}) for 0.5 h, and then cooled to 40 °C. The sample was heated from 40 °C to 600 °C with the rate of 5 °C·min^{–1} in 5% H₂/Ar (50 mL·min^{–1}). For the O₂-TPD process, 50 mg sample was treated with He gas at 105 °C for 0.5 h. Then, the sample was purged with 5% O₂/He (50 mL·min^{–1}) at room temperature for 0.5 h. After that, the sample was purged with He gas (50 mL·min^{–1}) for 0.5 h to remove the physisorbed O₂. Finally, the sample was heated from 40 °C to 900 °C with the rate of 5 °C·min^{–1} under the flow of He gas (50 mL·min^{–1}).

The diffuse reflectance infrared Fourier transform spectroscopy (DRIFTS) were characterized by Nicolet 6700 FTIR (Thermo Fisher, USA) equipped with a Harrick DRIFT cell and an MCT/A detector. The samples were pretreated in N₂ gas (50 mL·min^{–1}) at the set temperature for 1 h to stabilize the baseline. Then, 10 ppm of acetic acid gas (acetic acid/synthetic air) with 100 mL·min^{–1} was continuously introduced into the in-situ reaction chamber. The In-situ DRIFTS spectra was recorded at different temperature to detect the surface intermediates formed during acetic acid oxidation.

2.3. Catalytic activity test

The dynamic test was conducted in a quartz tubular reactor (Φ = 5 mm) with 100 mg catalyst (40–60 mesh). The reactor was placed in a pipe furnace, which can control the reaction temperature and maintain at each set temperature for 40 min. The composition of the reactant mixture was 1 ppm acetic acid containing synthetic air and water vapor, which was introduced via flowing synthetic air through a water bubbler at 28 °C with the saturated pressure of 3779.1 Pa. The relative humidity of mixed gas was 50%, thus the volume fraction of water vapor was 1.87%. The total flow was 100 mL·min^{–1}, corresponding to the weight hourly space velocity (WHSV) of 60 L·g^{–1}·h^{–1}. The concentrations of acetic acid and CO₂ was monitored online by GC-2014 (Shimadzu, Japan) equipped with a flame ionization detector (FID) and a methanizer. The acetic acid removal and conversion ratio to CO₂ was calculated according to the following equation:

$$\text{Acetic acid removal (\%)} = \frac{C_0 - C_t}{C_0} \times 100\% \quad (1)$$

$$\text{Conversion to CO}_2 \text{ (\%)} = \frac{C(\text{CO}_2)}{2 \times C_0} \times 100\% \quad (2)$$

where C_0 and C_t are the concentration of acetic acid in the inlet and outlet, respectively, and $C(\text{CO}_2)$ is the concentration of CO₂ in the outlet.

Besides, the static experiment was performed in a cuboid organic glass reactor with the volume of 4.5 L. 1.0 g of $\text{MnO}_2\text{-2H}$ was placed in a glass Petri dish with a glass cover. After the glass Petri dish with the catalyst was placed in the cuboid organic glass reactor, 2 μL acetic acid solution was injected into the reactor. With the help of 5 W fan inside the reactor, the acetic acid was volatilized. After the concentration was stabilized at ~ 25 ppm, the cover of the glass Petri dish was removed to let the catalyst exposed to acetic acid gas at room temperature (28°C , 1.50 vol% H_2O). The concentrations of acetic acid and CO_2 was monitored at intervals by GC-2014.

3. Results and discussion

3.1. Physicochemical properties of as-prepared sample

XRD patterns of the as-prepared samples with different acid treatment methods were compared. As shown in Fig. 1, $\text{MnO}_2\text{-NH}$, $\text{MnO}_2\text{-OH}$ and $\text{MnO}_2\text{-2H}$ all were birnessite-type MnO_2 with four weak diffraction peaks centered at 11.9° , 24.8° , 37.1° and 65.8° , corresponding to JCPDS 80–1098. From the FESEM, TEM and HRTEM images of $\text{MnO}_2\text{-NH}$ (Fig. 2A₁, B₁ and C₁), we can see that it consists of irregular MnO_2 nanoparticles with the average size of 5 nm. Moreover, because the catalyst was washed by cyclohexane, ethanol and calcined at 378 K to remove oleylamine, the MnO_2 nanoparticles seem to aggregate together. From its HRTEM image (Fig. 2D₁), we can see the lattice spacing of 0.248 nm and 0.253 nm which corresponds to the (110) and (200) planes of $\delta\text{-MnO}_2$ [32,33], with a cross angle of 60° , confirming {001} was the main exposed facet of $\text{MnO}_2\text{-NH}$. Similarly, $\text{MnO}_2\text{-OH}$ (Fig. 2D₂) and $\text{MnO}_2\text{-2H}$ (Fig. 2C₃) also mainly exposed {001} facets. The morphology of $\text{MnO}_2\text{-OH}$ was similar to that of $\text{MnO}_2\text{-NH}$ with the diagonal size of $\sim 5\text{--}10$ nm (Fig. 2A₂, B₂, C₂ and D₂) and consisted of many agglomerated $\delta\text{-MnO}_2$ nanoparticles. From the FESEM and HRTEM images of $\text{MnO}_2\text{-2H}$ (Fig. 2A₃, B₃, C₃ and D₃), it can be clearly seen that it consists of nanoribbons exposed {001} facets with the width of 5–10 nm and the length of 1–3 μm , leading to the aspect ratio as high as 200–600. The corresponding FFT pattern (inset of Fig. 2C₃) contains a set of strong $hk0$ diffraction spots arranged according to a pseudohexagonal symmetry, which can be attributed to the in-plane reflections of birnessite [33]. Moreover, as marked by a small red pane in Fig. 2D₃, the unbroken nanoribbons were found to have angular tips with a specific angle approximately equal to 120° , which correspond to the cross angle of two equivalent planes of (110) and ($\bar{1}10$), indicating that the nanoribbon was a single crystal, growing along the [010] direction, and the {110} facets served as the growth fronts due to their relatively higher surface energy. The thickness of $\text{MnO}_2\text{-2H}$ was investigated by the tapping-mode AFM image, as shown in Fig. 3, it was approximate

1–1.5 nm, suggesting a successful synthesis of ultrathin $\delta\text{-MnO}_2$ nanoribbons.

In the typical synthesis, $\delta\text{-MnO}_2$ UTNRs were synthesized by mixing the solution of KMnO_4 with OAm and EG, and adding H_2SO_4 at 2 h. Its growth is schemed in Fig. S1, before the addition of H_2SO_4 , the MnO_2 nanosheets formed through the redox between KMnO_4 and EG (Fig. S2A). While the $-\text{NH}_2$ groups of OAm are bound to the {001} facets, which acts as an end capping agent, and the long alkyl chain acts as a dispersant. After addition of H_2SO_4 , the reaction became violent and extremely promoted. As shown in Fig. S2, after H_2SO_4 added 5 and 30 min (Fig. S2B and C), the primary MnO_2 nanosheets begin to orientally attached together and form a string of beads, similar to reported in the literature [34]. The slight misalignment led to defect formation at the interface [34]. After added 1 and 2 h (Fig. S2D and E), through the continuous growth of crystals, the terrace of the interparticle boundary was gradually eliminated, and finally the ultrathin $\delta\text{-MnO}_2$ nanoribbons were obtained. Therefore, the long ultrathin $\delta\text{-MnO}_2$ nanoribbons were formed via edge-to-edge oriented attachment of primary MnO_2 nanosheets and further grown along the [010] direction with {001} facets exposed [35–38]. That is because the primary nanosheets have high surface energy, low K^+ content, and hydroxyl groups on edge sites that can form hydrogen bonding with the adjacent nanosheets [38]. What's more, due to the dissolution of some small nanosheets caused by acid treatment, the nanoribbons will also grow through dissolution-recrystallization mechanism, which has been proposed to explain the growth of various one-dimensional nanostructures [33]. The small nanosheets, with a higher free energy, was redissolved into the hydrothermal solution by acid treatment, then precipitated onto the surfaces of large nanosheets. The recrystallization would preferentially occur on the surface of {110} facets with higher surface energy. The continuous and rapid growth on these surfaces of large nanosheets lead to the formation of nanoribbons along the [010] direction. After reaction, the sample was filtered, washed several times with cyclohexane, ethanol, and deionized water to remove the remaining OAm and organic residues, the ultrathin nanoribbons aggregated and self-assembled into the network structure. FTIR spectra of the as-prepared samples are investigated. As shown in Fig. S3, no characteristic peak of NH_2 was observed. The strong peaks in the range of $500\text{--}600\text{ cm}^{-1}$ were ascribed to the vibrations of Mn-O bonds [39]. The peaks at 1630 cm^{-1} and 3390 cm^{-1} could be assigned to the OH stretching and bending vibrations, respectively [39]. The peaks at 1065 cm^{-1} and 1398 cm^{-1} were attributed to the bending vibrations of Mn-OH [27]. The peaks at 2892 cm^{-1} and 2982 cm^{-1} were ascribed to the C-H stretching vibrations [40]. In addition, the TOC of the as-prepared samples are also detected. The total organic carbon of $\text{MnO}_2\text{-NH}$, $\text{MnO}_2\text{-OH}$ and $\text{MnO}_2\text{-2H}$ was 0.13%, 0.11% and 0.12%, respectively. Therefore, it can be regarded that oleylamine was completely removed and only a very small amount of organic matter remained. Combined with the FESEM and AFM image of $\text{MnO}_2\text{-2H}$ (Figs. 2A₃ and 3), it can be verified that the space effect of network structure and disordered assembly enables the catalyst to maintain the dispersion of ultrathin nanoribbons without surfactant (OAm).

To ascertain the physicochemical properties of as-prepared catalysts, BET and XPS analysis were conducted. As shown in Table 1, the BET surface areas followed the order: $\text{MnO}_2\text{-2H}$ ($293\text{ m}^2\text{g}^{-1}$) > $\text{MnO}_2\text{-OH}$ ($134\text{ m}^2\text{g}^{-1}$) > $\text{MnO}_2\text{-NH}$ ($126\text{ m}^2\text{g}^{-1}$) calculated from the nitrogen adsorption curves (Fig. S4A). It can be seen that $\text{MnO}_2\text{-2H}$ has the largest specific surface area and pore volume, which is consistent with previous reports that the network structure has the advantages of large specific surface area, high porosity, high mass transfer efficiency and abundant adsorption/activation sites [41–45]. All the as-prepared samples belong to the type IV with a distinct H3 hysteresis loop, corresponding to slit pores. Combined with FESEM (Fig. 2A₃), the network structure of $\text{MnO}_2\text{-2H}$ makes it have more slit pores, which is consistent with DFT pore size distributions (Fig. S4B). The pore size of all as-prepared samples mainly centered at ~ 4.9 nm.

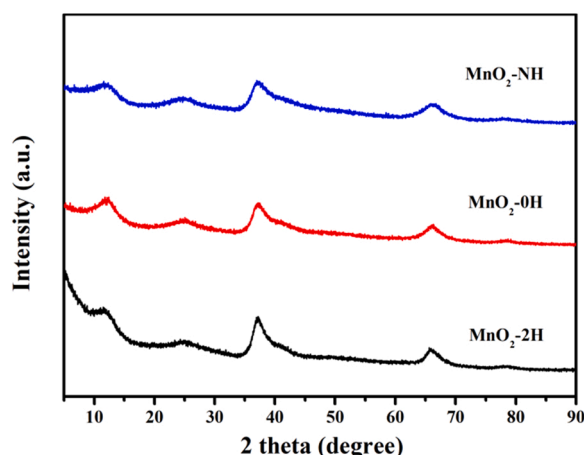


Fig. 1. X-ray diffraction patterns of as-prepared MnO_2 catalysts.

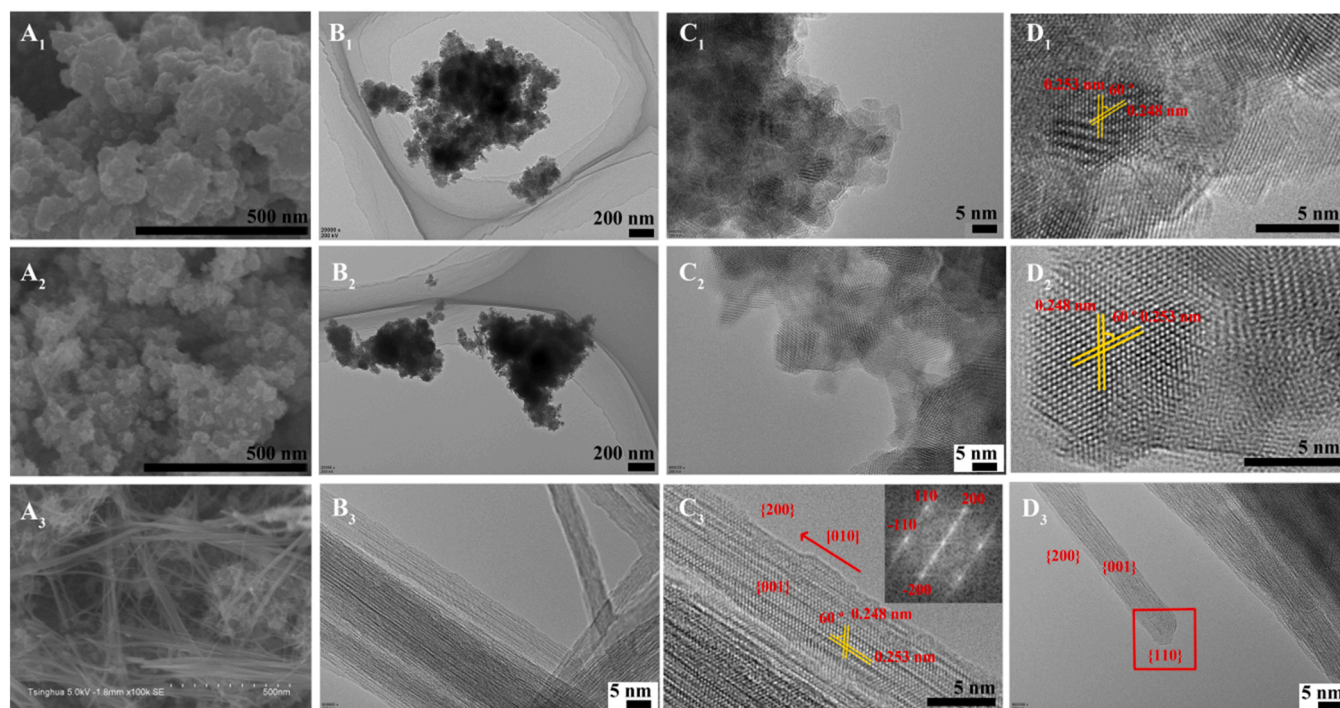


Fig. 2. FESEM, TEM and HRTEM images of (A₁, B₁, C₁ and D₁) MnO₂-NH, (A₂, B₂, C₂ and D₂) MnO₂-OH and (A₃, B₃, C₃ and D₃) MnO₂-2H. Inset is the corresponding fast Fourier transform (FFT) pattern of the nanoribbons surface.

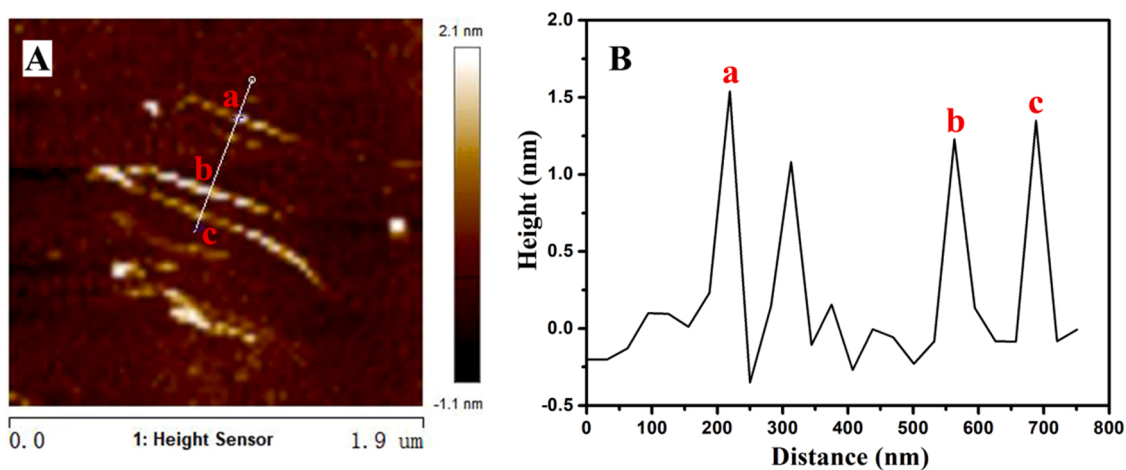


Fig. 3. Tapping-mode AFM image of MnO₂-2H. (B) Height profile along the line in (A).

Table 1

BET surface area and XPS results of the as-prepared samples.

	BET (m ² / g)	Pore volume (cm ³ /g)	K/ Mn	Mn/O	AOS	O _{ads} / O _{latt}	Mn ⁴⁺ / Mn ³⁺
MnO ₂ - NH	126	0.207	0.49	0.97:2	3.58	0.19	1.12
MnO ₂ - OH	134	0.258	0.39	1.01:2	3.60	0.24	1.16
MnO ₂ - 2H	293	0.527	0.28	1.03:2	3.63	0.27	1.20

XPS spectra of the as-prepared samples are shown in Fig. 4. The XPS survey spectra (Fig. 4A) shows that the main elements of the as-prepared samples are Mn, O and K. There is no N in XPS survey spectra, which proved that oleylamine was completely removed. Similar to those

reported in the literature [46], the Mn 3s spectra split due to the parallel spin coupling between the 3d and the 3s electron during the photoelectron ejection. Thus, the average oxidation state (AOS) of Mn was calculated according to the Mn 3s multiplet splitting energy (ΔE), i.e. $AOS = 8.956 - 1.126 \times \Delta E$ [27] (Fig. 4B). As shown in Table 1, MnO₂-2H shows a higher AOS (3.63) than that of MnO₂-OH (3.60) and MnO₂-NH (3.58). The Mn 2p_{3/2} spectra (Fig. 4C) could be divided into three peaks corresponding to the surface Mn³⁺ (642.3 eV), Mn⁴⁺ (642.9 eV) species and the satellite peak (645.6 eV) [47], respectively. Moreover, it can be seen that in comparison with the peaks of MnO₂-OH and MnO₂-NH centered at 642.3 eV and 642.9 eV, those of MnO₂-2H shifted towards higher binding energy values (642.4 eV and 643.0 eV), implying that the surrounding chemical environment of Mn in MnO₂-2H is different from other two samples owing to the generation of the charge imbalance, oxygen vacancies and Mn⁴⁺ species in the structure [47]. The proportion of Mn⁴⁺/Mn³⁺ follows the order (Table 1): MnO₂-2H (1.20)

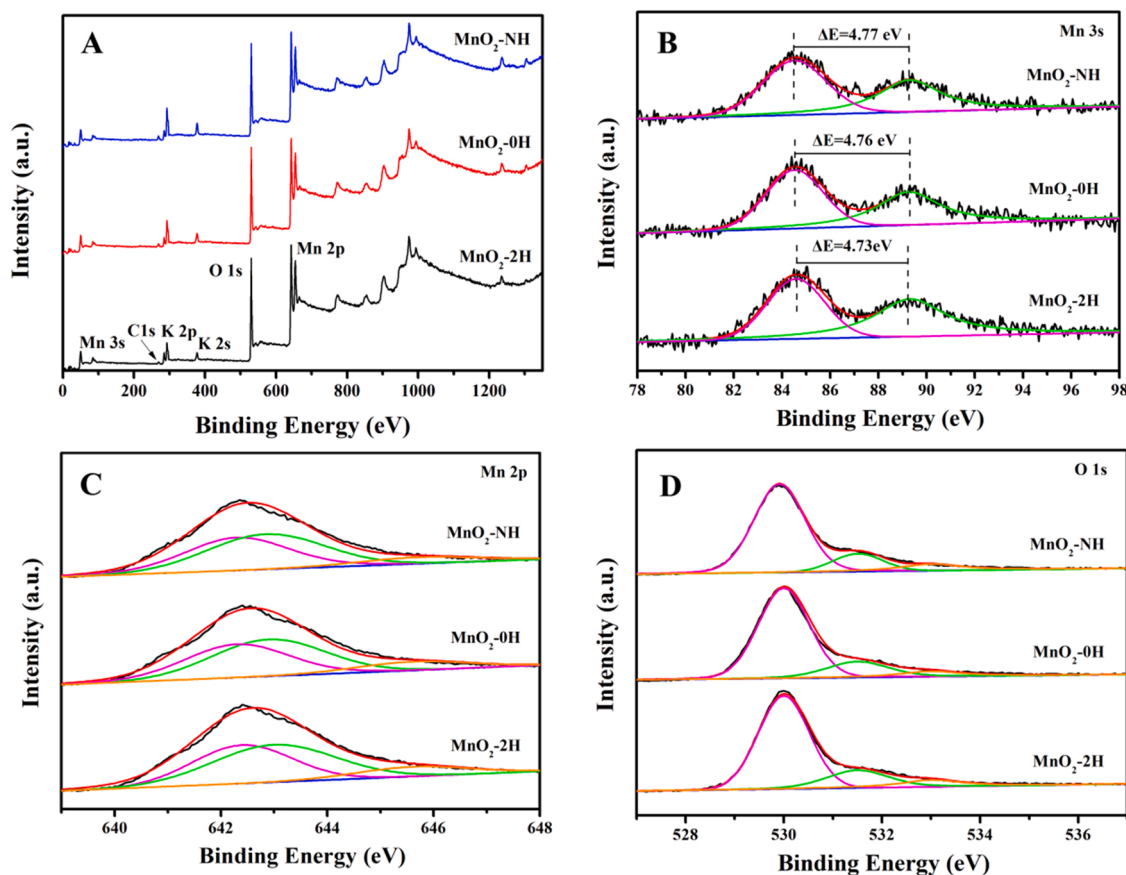


Fig. 4. XPS spectra of (A) survey spectra, (B) Mn 3s, (C) Mn 2p, (D) O 1s of as-prepared samples.

> $\text{MnO}_2\text{-OH}$ (1.16) > $\text{MnO}_2\text{-NH}$ (1.12). The acid treated catalysts exhibited the relatively high amount of surface Mn^{4+} probably due to the disproportionation of Mn^{3+} induced by acid treatment [48,49]. So, the increase of Mn^{4+} suggested the existence of more vacancy defects on the surface of $\text{MnO}_2\text{-2H}$, which may lead to the charge imbalance, resulting in a large number of adsorbed oxygen species and unsaturated chemical bonds on the catalyst surface, in which more weakly adsorbed oxygen is more efficient than bulk lattice oxygen owing to its much higher migration [50]. The interlayer K^+ ions play a significant role in balancing the charge in MnO_2 . The K/Mn proportion (Table 1) followed the order: $\text{MnO}_2\text{-NH}$ (0.49) > $\text{MnO}_2\text{-OH}$ (0.39) > $\text{MnO}_2\text{-2H}$ (0.28). It can be seen that addition of sulfuric acid decreased the K^+ content due to replacing of K^+ by H^+ . $\text{MnO}_2\text{-2H}$ had the lowest K content, which is consistent with its ultrathin thickness ($\sim 1\text{--}1.5$ nm).

The O 1s spectrum of the samples (Fig. 4D) can be divided into three peaks located at 530.0 eV, 531.5 eV and 533.1 eV, corresponding to lattice oxygen (O_{latt}), surface adsorbed oxygen (O_{ads}) and surface adsorbed water ($\text{O}_{\text{adsH}_2\text{O}}$), respectively [50,51]. The $\text{O}_{\text{ads}}/\text{O}_{\text{latt}}$ proportion followed the order: $\text{MnO}_2\text{-2H}$ (0.27) > $\text{MnO}_2\text{-OH}$ (0.24) > $\text{MnO}_2\text{-NH}$ (0.19) (Table 1), implying that $\text{MnO}_2\text{-2H}$ had the highest amount of oxygen vacancies. This result can be ascribed to the acid treatment which would accelerate the disproportionation of Mn^{3+} and induce the catalyst to expose abundant defects to capture more surface adsorbed molecular oxygen [40,48].

The Raman spectra of the as-prepared samples are shown in Fig. S5. Three major peaks in the range of $500\text{--}650\text{ cm}^{-1}$ appeared in all samples. The peak near 507 cm^{-1} was associated with the deformation modes of Mn-O, and peaks near 580 cm^{-1} and 625 cm^{-1} were assigned to the stretching vibration of the Mn-O [39]. Compared to $\text{MnO}_2\text{-NH}$ (583.5 cm^{-1}) and $\text{MnO}_2\text{-OH}$ (581.4 cm^{-1}), peak around 580 cm^{-1} of $\text{MnO}_2\text{-2H}$ shifted to 577.5 cm^{-1} . This shift was ascribed to the enriching

of crystal defects and lattice distortion in $\text{MnO}_2\text{-2H}$, which is consistent with the results of XPS.

$\text{H}_2\text{-TPR}$ and $\text{O}_2\text{-TPD}$ were also performed to evaluate the redox ability of the as-prepared sample. $\text{H}_2\text{-TPR}$ profiles of the catalysts are shown in Fig. 5A, the reduction temperature of $\text{MnO}_2\text{-2H}$ (291°C) is lower than that of $\text{MnO}_2\text{-NH}$ (310°C) and $\text{MnO}_2\text{-OH}$ (300°C). This result is consistent with the ratio of high-valence species (Mn^{4+}) among the three $\delta\text{-MnO}_2$ samples revealed by XPS. As shown in Fig. 5B, the $\text{O}_2\text{-TPD}$ spectra can be divided into three regions: surface active oxygen ($< 300^\circ\text{C}$), subsurface lattice oxygen ($300\text{--}600^\circ\text{C}$) and bulk lattice oxygen ($> 600^\circ\text{C}$) [40], respectively. Oxygen vacancy sites may be occupied by the dioxygen and to form surface adsorbed oxygen, which mainly contributes to the signal below 300°C in $\text{O}_2\text{-TPD}$ [32,40]. $\text{MnO}_2\text{-2H}$ contributes the lowest desorption temperature (178°C) and the highest amount of adsorbed oxygen species among the three samples, which further confirms the existence of abundant oxygen vacancies on $\text{MnO}_2\text{-2H}$. In addition, the desorption temperature of subsurface lattice oxygen for $\text{MnO}_2\text{-2H}$ (498°C) is lower than that of $\text{MnO}_2\text{-NH}$ (589°C) and $\text{MnO}_2\text{-OH}$ (533°C), implying that $\text{MnO}_2\text{-2H}$ has the highest oxygen mobility among three samples. So, the subsurface lattice oxygen in $\text{MnO}_2\text{-2H}$ is more easily to participate in acetic acid oxidation [27,32].

ESR was also used to determine whether any radicals existed on as-synthesized samples by using DMPO as the trapping agent. As shown in Fig. 6A and B, the characteristic 1:2:2:1 four-peak signal of $\text{DMPO}\cdot\text{OH}$ adducts and 1:1:1:1 four-peak signal of $\text{DMPO}\cdot\text{O}_2^-$ adducts [52, 53] were detected, indicating the existence of hydroxyl radicals ($\cdot\text{OH}$) and superoxide radicals ($\cdot\text{O}_2^-$) on as-prepared samples. Among all the samples, $\text{MnO}_2\text{-2H}$ shows the strongest signals of both radicals, manifesting that it owned the largest amount of oxygen vacancies, which is in good agreement with the $\text{H}_2\text{-TPR}$, $\text{O}_2\text{-TPD}$ and XPS results. These results imply $\text{MnO}_2\text{-2H}$ may exhibit much higher catalytic activity than other

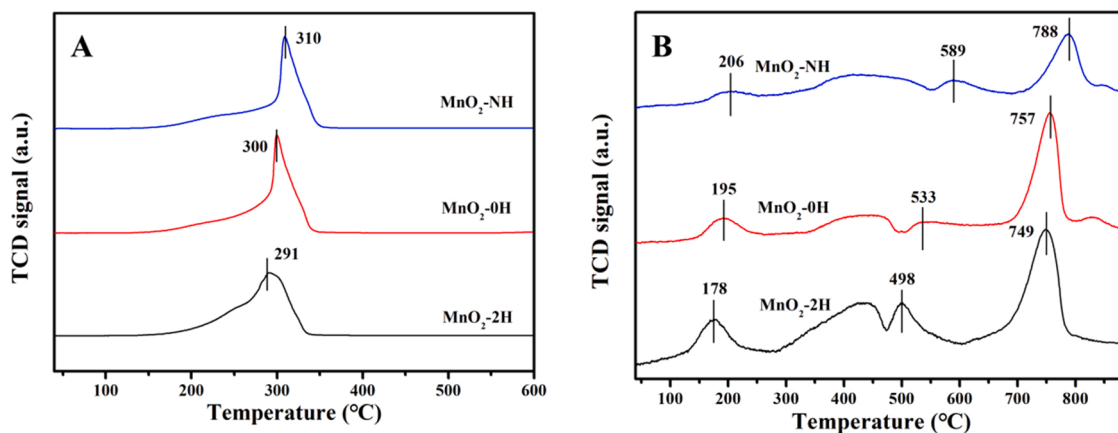


Fig. 5. (A) H_2 -TPR and (B) O_2 -TPD profiles of as-prepared samples.

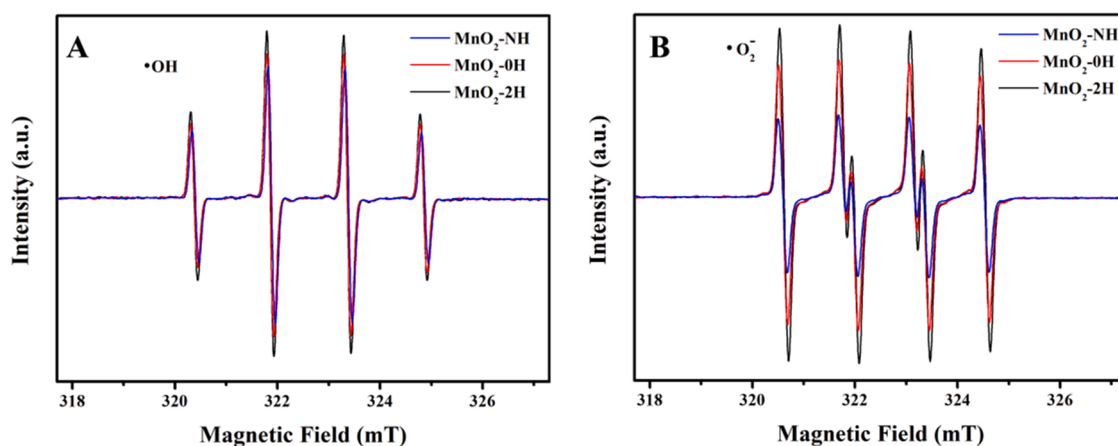


Fig. 6. ESR spectra of as-prepared samples in (A) H_2O and (B) DMSO by using DMPO as trapping agent.

two samples.

3.2. Activity for acetic acid removal

The catalytic performance of as-prepared samples for low concentration acetic acid (1 ppm) was carried out under the WHSV of $60 \text{ L} \cdot \text{g}^{-1} \cdot \text{h}^{-1}$ and 1.87 vol% H_2O . As shown in Fig. 7A, even at room temperature, all three samples achieved 100% removal of acetic acid. However, the conversion ratio to CO_2 greatly increased with the increase

of the reaction temperature when the temperature was below 130°C . And below 130°C , the conversion ratio to CO_2 follows the order of $\text{MnO}_2\text{-2H} > \text{MnO}_2\text{-0H} > \text{MnO}_2\text{-NH}$, which is consistent with the orders of radicals, oxygen vacancies and the ratio of $\text{Mn}^{4+}/\text{Mn}^{3+}$. $\text{MnO}_2\text{-2H}$ exhibited the highest activity to transform acetic acid into CO_2 . For example, at 120°C , $\text{MnO}_2\text{-2H}$ converted 95% acetic acid to CO_2 , while $\text{MnO}_2\text{-0H}$ and $\text{MnO}_2\text{-NH}$ achieved 80% and 41%, respectively. In addition, the rate of conversion to CO_2 by $\text{MnO}_2\text{-NH}$, $\text{MnO}_2\text{-0H}$ and $\text{MnO}_2\text{-2H}$ at 100°C was 2.66×10^{-5} , 7.14×10^{-5} and 8.95×10^{-5}

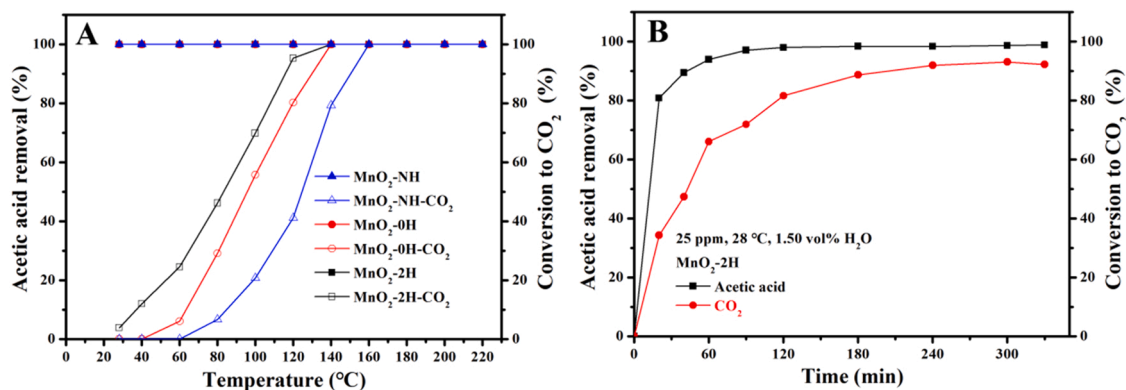


Fig. 7. (A) The dynamic removal of acetic acid and conversion to CO_2 by as-prepared samples at different temperature (inlet acetic acid concentration: 1 ppm, WHSV: $60 \text{ L} \cdot \text{g}^{-1} \cdot \text{h}^{-1}$, 1.87 vol% H_2O). (B) The static removal of acetic acid and conversion to CO_2 by $\text{MnO}_2\text{-2H}$ at room temperature (acetic acid concentration: 25.41 ppm, 28°C , 1.50 vol% H_2O).

$\text{mol}\cdot\text{L}^{-1}\cdot\text{s}^{-1}$, respectively. And their corresponding $O_{\text{ads}}/O_{\text{latt}}$ is 0.19, 0.24 and 0.27 (Table 1). As shown in Fig. S6A, the rate of conversion to CO_2 is linear to the $O_{\text{ads}}/O_{\text{latt}}$ ratio, indicating some quantitative relation between the reaction rate with oxygen vacancies, as well as the properties of H_2 -TPR and O_2 -TPD. However, as shown in Fig. S6B, the rate of conversion to CO_2 is not linear to the specific surface area, indicating the higher activity of $\text{MnO}_2\text{-2H}$ is not just due to its higher surface area. As we know, the VOCs oxidation involves many steps including adsorption, reaction and desorption, the general and accurate relation needs more deep investigation. During the dynamic experiment, the gaseous intermediates such as CO was not detected with the GC-FID directly or by GC-FID with a methanizer at all temperatures as shown in Fig. S7. According to the above results, we conclude that at low temperature, the conversion of acetic acid to CO_2 become slow, and acetic acid mostly adsorbed on the surface of catalyst, as well as its intermediates.

Both $\bullet\text{OH}$ and $\bullet\text{O}_2^-$ were detected in all three samples (Fig. 6), and their relative strength is consistent with their activity for acetic acid decomposition (Fig. 7A). In order to verify the role of $\bullet\text{OH}$ and $\bullet\text{O}_2^-$ in catalytic oxidation process, the effect of *tert*-butanol on the removal of acetic acid by $\text{MnO}_2\text{-2H}$ was investigated. *tert*-butanol is a scavenger of hydroxyl radicals in aqueous solution. As shown in Fig. S8B, when *tert*-butanol (1.1 ppm) was coexistent with acetic acid (1.3 ppm), the removal ratio of acetic acid did not change keeping 100% at all temperatures. And at temperatures higher than 140°C , not only acetic acid but also *tert*-butanol were completely converted into CO_2 . However, when the temperature reduced to 120°C , the conversion to CO_2 decreased to about 50%; and at 60°C , no CO_2 was produced. While in the absence of *tert*-butanol, at 120°C , most acetic acid was converted into CO_2 , and at 60°C generation of CO_2 was obvious (Fig. S8A). The above results indicate the presence of low concentration *tert*-butanol did inhibit the conversion of acetic acid to CO_2 , confirming the role of hydroxyl radicals in the conversion of acetic acid to CO_2 . On the other side, the result of no effect of *tert*-butanol at temperatures higher than 140°C may be ascribed to the role of superoxide in the conversion of acetic acid to CO_2 . Thus, according to the present results, we conclude that these two kinds of radicals participate in the oxidation of acetic acid.

Under the dynamic test, we see the conversion to CO_2 at room temperature was low. To verify whether $\text{MnO}_2\text{-2H}$ could transform acetic acid into CO_2 at room temperature, the static removal and conversion experiment was conducted at 28°C in the presence of 1.50 vol % H_2O . As shown in Fig. 7B, the concentration of acetic acid soon decreased 80% within first 20 min, and the corresponding conversion to CO_2 reached over 35%. And during the whole reaction period, the removal of acetic acid and its conversion ratio to CO_2 was about 98% and 93%, respectively. The above results demonstrate that as-synthesized $\text{MnO}_2\text{-2H}$ can transform acetic acid into CO_2 at room temperature, however the conversion rate of acetic acid to CO_2 is much

slower than the removal rate of itself.

Thus, we further checked the removal capacity of $\text{MnO}_2\text{-2H}$ for low concentration acetic acid at room temperature (28°C). Under the WHSV of $600\text{ L}\cdot\text{g}^{-1}\cdot\text{h}^{-1}$ (the corresponding residence time was 0.035 s) and 1.87 vol% H_2O , $\text{MnO}_2\text{-2H}$ kept 100% removal of 1.23 ppm acetic acid within 11.5 h and then the removal ratio decreased (Fig. 8A). The corresponding 100% removal capacity was calculated as high as 20.84 mg/g, which was much higher than that of $\text{MnO}_2\text{-NH}$ (10.87 mg/g). After $\text{MnO}_2\text{-2H}$ was regenerated at 140°C for 1 h, it was reused for removing acetic acid at 28°C . It can be seen its removal capacity was well recovered, reaching 21.74 mg/g. After the second and third regeneration and reuse, the 100% removal capacity was 19.03 mg/g and 19.93 mg/g, respectively. The above results manifest that the $\text{MnO}_2\text{-2H}$ can be effectively regenerated at 140°C and has good reusability. Its stability at high temperature (140°C) was also tested in the presence of 1.87 vol% H_2O (Fig. 8B), both acetic acid removal and its conversion to CO_2 kept 100% within 50 h, demonstrating its high stability and water resistant at high temperature.

3.3. Acetic acid decomposition pathway

To learn the decomposition pathway of acetic acid and its intermediates, the in-situ DRIFTS of acetic acid over the as-prepared samples was conducted. The in-situ DRIFTS of $\text{MnO}_2\text{-NH}$ at 30°C is shown in Fig. 9A, the peaks of 1702 cm^{-1} and 1652 cm^{-1} were characteristic absorption of carbonyl stretching. The weak peak at 1702 cm^{-1} indicated that some of acetic acid was adsorbed with hydrogen bonding, which may come from the interaction of an adsorbed acetic acid with catalyst surface OH groups or with other acetic acid molecule [54]. The peak at 1652 cm^{-1} was attributed to acetic acid bonded at Lewis acid sites (Mn^{4+}) through the oxygen lone-pair electrons of the carbonyl group [54]. It can be seen that the typical carboxyl peaks at 1582 cm^{-1} , 1417 cm^{-1} and 1345 cm^{-1} increased with exposure time, indicating the increasing adsorption of acetic acid on the surface of the catalyst [32,40,54–57]. In DRIFT spectra of HCOONa , CH_3COONa and CH_3COOH mixed with KBr (Fig. 9B), the characteristic vibration peaks of formic acid were 1604 cm^{-1} and 1363 cm^{-1} , and those of acetic acid were 1558 cm^{-1} and 1412 cm^{-1} . Thus, the peaks of 1582 cm^{-1} and 1417 cm^{-1} can be attributed to the asymmetrical and symmetrical stretching of the adsorbed acetic acid carboxyl group, and the weak peak of 1345 cm^{-1} was attributed to the vibration peak of formic acid, implying formic acid was an intermediate during acetic acid decomposition. What's more, the $\Delta\nu$ value of carboxyl group of acetic acid on $\text{MnO}_2\text{-NH}$ was 165 cm^{-1} , which was substantially greater than that of its sodium salt (146 cm^{-1}). According to the literature [58], the above result indicates CH_3COOH adsorbed to $\text{MnO}_2\text{-NH}$ via its carboxylate group in a unidentate mode. The strong peak at 3567 cm^{-1} and

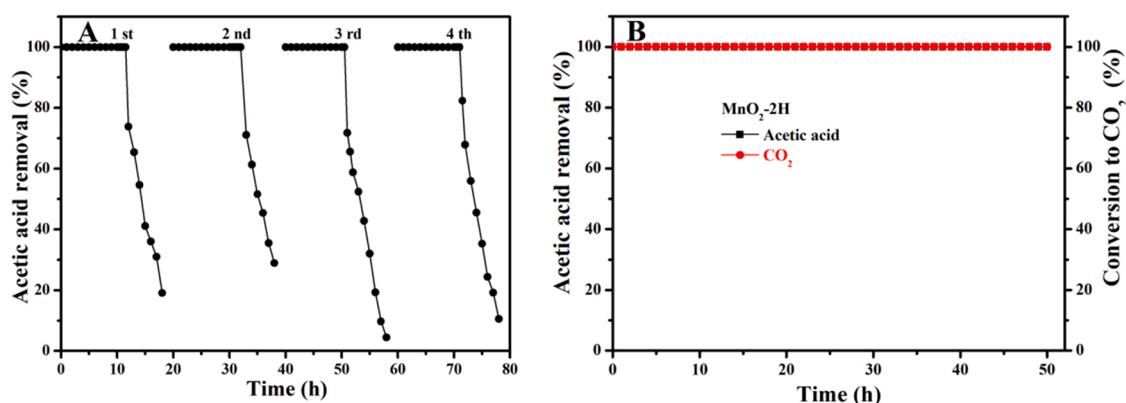


Fig. 8. (A) The removal of acetic acid by $\text{MnO}_2\text{-2H}$ at room temperature (inlet acetic acid concentration: 1.23 ppm, WHSV: $600\text{ L}\cdot\text{g}^{-1}\cdot\text{h}^{-1}$, 1.87 vol% H_2O), $\text{MnO}_2\text{-2H}$ was regenerated at 140°C for 1 h in oven. (B) The stability of $\text{MnO}_2\text{-2H}$ during catalytic removal of acetic acid at 140°C (inlet acetic acid concentration: 1 ppm, WHSV: $60\text{ L}\cdot\text{g}^{-1}\cdot\text{h}^{-1}$, 1.87 vol% H_2O).

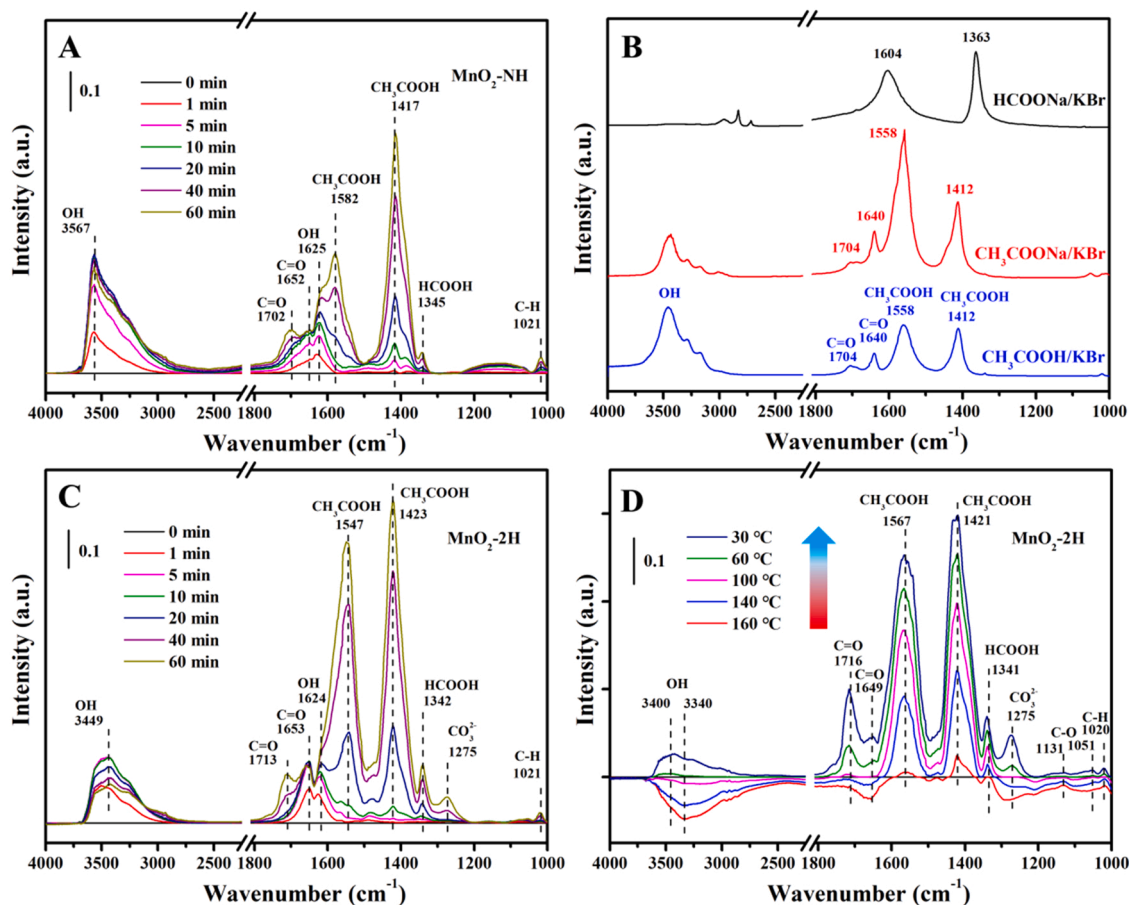


Fig. 9. In-situ DRIFT spectra of as-prepared samples exposed to the flow of 10 ppm acetic acid (WHSV: 60 L·g⁻¹·h⁻¹, 1.87 vol% H₂O). (A) MnO₂-NH at 30 °C; (C) MnO₂-2H at 30 °C; (D) MnO₂-2H under series of temperature; (B) DRIFT spectra of HCOONa, CH₃COONa and CH₃COOH mixed with KBr.

1625 cm⁻¹ are ascribed to structural vibrations of OH groups on the catalyst surface, including physically adsorbed bound water and chemically adsorbed hydroxyl groups [28,43,45]. The small peak at 1021 cm⁻¹ belonged to the stretching vibration of C-H bands [32].

The in-situ DRIFTS of MnO₂-2H under the same conditions are shown in Fig. 9C. In comparison with MnO₂-NH, the carboxyl characteristic peaks of 1547 cm⁻¹, 1423 cm⁻¹ and 1342 cm⁻¹ were significantly enhanced, indicating that MnO₂-2H has stronger adsorption ability for acetic acid and low-temperature conversion ability. Meanwhile, the stretching vibration at 1275 cm⁻¹ ascribed to carbonate (CO₃²⁻) [9,59] occurred, which further proved that MnO₂-2H had better catalytic activity than MnO₂-NH. The OH peak of MnO₂-2H at 3449 cm⁻¹ was significantly weaker than that of MnO₂-NH (3567 cm⁻¹), and its intensity increased from 0 min to 5 min and decreased from 5 min to 60 min, indicating that MnO₂-2H has better water resistance, and the OH group on the catalyst surface was consumed during the removal of acetic acid. During reaction, H₂O would be adsorbed on oxygen vacancy and dissociated into new active oxygen species. However, oxygen vacancy site is the main reaction site for acetic acid oxidation. The competitive adsorption of water with acetic acid could reduce the contact and residence of acetic acid on the catalyst surface and thereby lower catalytic activity of the catalyst. In addition, the $\Delta\nu$ value of carboxyl asymmetrical and symmetrical stretching of MnO₂-2H (124 cm⁻¹) was smaller than ionic $\Delta\nu$, implying that CH₃COOH was chemically adsorbed to Mn atom of MnO₂-2H via carboxyl group in a bidentate or bridging configuration [58]. Compared with the adsorption of MnO₂-NH via unidentate mode, the bidentate or bridging configuration made acetic acid more easily adsorbed to MnO₂-2H, which is beneficial for acetic acid to be decomposed [58]. Accordingly, MnO₂-2H

possesses much higher activity than MnO₂-NH to decompose acetic acid.

The temperature dependent in-situ DRIFTS of MnO₂-2H under the flow of acetic acid is shown in Fig. 9D. It can be seen that with the decrease of temperature, the organic species adsorbed on the surface of MnO₂-2H were acetic acid (1567 cm⁻¹ and 1421 cm⁻¹), formic acid (1341 cm⁻¹) and carbonate (1275 cm⁻¹), in which acetic acid was the main component. Therefore, the transform of acetic acid into formic acid is believed as the rate-determining step. According to the in-situ DRIFTS results, the decomposition pathway of acetic acid is proposed as in Fig. 10. First acetic acid fast adsorbs on the surface of MnO₂-2H in a bidentate or bridging configuration, and then acetic acid is oxidized with oxygen species such as $\bullet\text{O}_2^-$ and $\bullet\text{OH}$ to decarboxylate its carboxyl group, resulting in formation of formic acid. Next, formic acid is further oxidized with oxygen species to form carbonate. Finally, carbonate is desorbed from the surface to release CO₂ and H₂O.

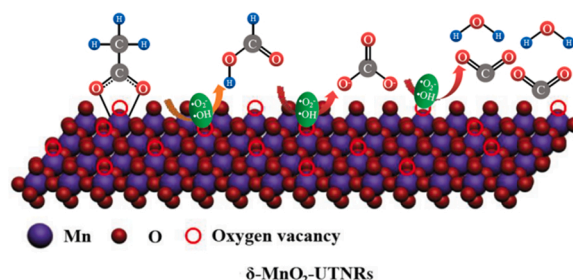


Fig. 10. Proposed mechanism for acetic acid oxidation on δ -MnO₂ UTNRs.

4. Conclusions

In summary, the ultrathin δ -MnO₂ nanoribbons was successfully prepared via a convenient redox between KMnO₄ and ethylene glycol adjusted by oleylamine and sulfuric acid. The few-layers nanoribbons with exposure of {001} facets were self-assembled into the network structure, which is favorable for the mass transfer and water vapor penetration. As-prepared δ -MnO₂ UTNRs owned a lot of defects and oxygen vacancies, thus many active oxygen species such as hydroxyl radicals and superoxide existed on its surface. In combination with its high specific surface area, δ -MnO₂ UTNRs exhibited significant catalytic activity and can transform the human-related odorant - acetic acid into CO₂ even at room temperature. In-situ DRIFTS results indicate that acetic acid first adsorbed to δ -MnO₂ UTNRs via its carboxylate group in the bidentate or bridging mode, and then decarboxylated and further oxidized into formic acid, carbonate and CO₂. The δ -MnO₂ UTNRs accumulated with acetic acid and its intermediate could be completely regenerated at 140 °C for reuse.

CRediT authorship contribution statement

Tongzhou Xu: Conceptualization, Methodology, Visualization, Investigation, Formal analysis, Data curation, Writing – original draft.
Pengyi Zhang: Supervision, Writing – review & editing.
Huiyu Zhang: Resources, Formal analysis.

Declaration of Competing Interest

The authors declare that they have no known competing financial interests or personal relationships that could have appeared to influence the work reported in this paper.

Acknowledgment

This work was supported by the Science and Technology Innovation Program of Shunde of Foshan City (No. 2130218002526).

Appendix A. Supporting information

Supplementary data associated with this article can be found in the online version at doi:10.1016/j.apcatb.2022.121273.

References

- [1] J. Spengler, K. Sexton, Indoor air pollution: a public health perspective, *Science* 221 (1983) 9–17.
- [2] K.S. Dwi, K. Sachi, T. Yasuhiro, H. Hajime, K. Naoki, A. Keiichi, F. Hidekazu, S. Fumihiko, Effect of prolonged exposure to low concentrations of formaldehyde on the corticotropin releasing hormone neurons in the hypothalamus and adrenocorticotrophic hormone cells in the pituitary gland in female mice, *Brain Res.* 1013 (2004) 107–116.
- [3] J.C. Little, A.T. Hodgson, A.J. Gadgil, Modeling emissions of volatile organic compounds from new carpets, *Atmos. Environ.* 28 (1994) 227–234.
- [4] J. Mo, Y. Zhang, Q. Xu, Y. Zhu, J.J. Lamson, R. Zhao, Determination and risk assessment of by-products resulting from photocatalytic oxidation of toluene, *Appl. Catal. B* 89 (2009) 570–576.
- [5] T. Xu, H. Zheng, P. Zhang, Isolated Pt single atomic sites anchored on nanoporous TiO₂ film for highly efficient photocatalytic degradation of low concentration toluene, *J. Hazard. Mater.* 388 (2020), 121746.
- [6] H. Guo, S.C. Lee, L. Chan, W. Li, Risk assessment of exposure to volatile organic compounds in different indoor environments, *Environ. Res.* 94 (2004) 0–66.
- [7] Y. Liu, P.K. Misztal, J. Xiong, Y. Tian, C. Arata, R.J. Weber, W.W. Nazaroff, A. H. Goldstein, Characterizing sources and emissions of volatile organic compounds in a northern California residence using space-and time-resolved measurements, *Indoor Air* 29 (2019) 630–644.
- [8] J. Wang, P. Zhang, J. Li, C. Jiang, R. Yunus, J. Kim, Room-temperature oxidation of formaldehyde by layered manganese oxide: effect of water, *Environ. Sci. Technol.* 49 (2015) 12372–12379.
- [9] H. Zhang, X. Zheng, T. Xu, P. Zhang, Atomically dispersed Y or La on birnessite-type MnO₂ for the catalytic decomposition of low-concentration toluene at room temperature, *ACS Appl. Mater. Inter.* 13 (2021) 17532–17542.
- [10] C. Cellier, S. Lambert, E.M. Gaigneaux, C. Poleunis, V. Ruaux, P. Eloy, C. Lahousse, P. Bertrand, J.P. Pirard, P. Grange, Investigation of the preparation and activity of gold catalysts in the total oxidation of *n*-hexane, *Appl. Catal. B* 70 (2007) 406–416.
- [11] C. Lahousse, A. Bernier, P. Grange, B. Delmon, P. Papaefthimiou, T. Ioannides, X. Verykios, Evaluation of γ -MnO₂ as a VOC removal catalyst: comparison with a noble metal catalyst, *J. Catal.* 178 (1998) 214–225.
- [12] C. Cellier, V. Ruaux, C. Lahousse, P. Grange, E.M. Gaigneaux, Extent of the participation of lattice oxygen from γ -MnO₂ in VOCs total oxidation: influence of the VOCs nature, *Catal. Today* 117 (2006) 350–355.
- [13] International Energy Agency, Energy Efficiency 2020, 2020.
- [14] International Energy Agency, Net Zero by 2050-A Roadmap for the Global Energy Sector, 2021.
- [15] X. Zhang, P. Wargocki, Z. Lian, C. Thyregod, Effects of exposure to carbon dioxide and bioeffluents on perceived air quality, self-assessed acute health symptoms, and cognitive performance, *Indoor Air* 27 (2017) 47–64.
- [16] X. Tang, P.K. Misztal, W.W. Nazaroff, A.H. Goldstein, Volatile organic compound emissions from humans indoors, *Environ. Sci. Technol.* 50 (2016) 12686–12694.
- [17] S. Liu, S.L. Thompson, H. Stark, P.J. Ziemann, J.L. Jimenez, Gas-phase carboxylic acids in a university classroom: abundance, variability, and sources, *Environ. Sci. Technol.* 51 (2017) 5454–5463.
- [18] P. Wolkoff, C.K. Wilkins, P.A. Clausen, G.D. Nielsen, Organic compounds in office environments-sensory irritation, odor, measurements and the role of reactive chemistry, *Indoor Air* 16 (2006) 7–19.
- [19] J. Guo, C. Lin, C. Jiang, P. Zhang, Review on noble metal-based catalysts for formaldehyde oxidation at room temperature, *Appl. Surf. Sci.* 475 (2019) 237–255.
- [20] L. Miao, J. Wang, P. Zhang, Review on manganese dioxide for catalytic oxidation of airborne formaldehyde, *Appl. Surf. Sci.* 466 (2019) 441–453.
- [21] Y. Liu, W. Yang, P. Zhang, J. Zhang, Nitric acid-treated birnessite-type MnO₂: an efficient and hydrophobic material for humid ozone decomposition, *Appl. Surf. Sci.* 442 (2018) 640–649.
- [22] R. Cao, P. Zhang, Y. Liu, X. Zheng, Ammonium-treated birnessite-type MnO₂ to increase oxygen vacancies and surface acidity for stably decomposing ozone in humid condition, *Appl. Surf. Sci.* 495 (2019), 143607.
- [23] P. Wu, X. Jin, Y. Qiu, D. Ye, Recent progress of thermocatalytic and photo/thermocatalytic oxidation for VOCs purification over manganese-based oxide catalysts, *Environ. Sci. Technol.* 55 (2021) 4268–4286.
- [24] J. Zhang, Y. Li, L. Wang, C. Zhang, H. He, Catalytic oxidation of formaldehyde over manganese oxides with different crystal structures, *Catal. Sci. Technol.* 5 (2015) 2305–2313.
- [25] S. Selvakumar, N. Nuns, M. Trentesaux, V.S. Batra, J.M. Giraudon, J.F. Lamonier, Reaction of formaldehyde over birnessite catalyst: a combined XPS and ToF-SIMS study, *Appl. Catal. B* 223 (2018) 192–200.
- [26] S. Rong, P. Zhang, J. Wang, F. Liu, Y. Yang, G. Yang, S. Liu, Ultrathin manganese dioxide nanosheets for formaldehyde removal and regeneration performance, *Chem. Eng. J.* 306 (2016) 1172–1179.
- [27] R. Cao, L. Li, P. Zhang, L. Gao, S. Rong, Regulating oxygen vacancies in ultrathin δ -MnO₂ nanosheets with superior activity for gaseous ozone decomposition, *Environ. Sci. Nano* 8 (2021) 1628–1641.
- [28] H. Zhang, S. Sui, X. Zheng, R. Cao, P. Zhang, One-pot synthesis of atomically dispersed Pt on MnO₂ for efficient catalytic decomposition of toluene at low temperatures, *Appl. Catal. B* 257 (2019), 117878.
- [29] S. Rong, K. Li, P. Zhang, F. Liu, J. Zhang, Potassium associated manganese vacancy in birnessite-type manganese dioxide for airborne formaldehyde oxidation, *Catal. Sci. Technol.* 8 (2018) 1799–1812.
- [30] J. Wang, G. Zhang, L. Ren, L. Kang, Z. Hao, Z. Lei, Z.H. Liu, Topochemical oxidation preparation of regular hexagonal manganese oxide nanoplates with birnessite-type layered structure, *Cryst. Growth Des.* 14 (2014) 5626–5633.
- [31] K.A.M. Ahmed, K. Huang, Synthesis, characterization and catalytic activity of birnessite type potassium manganese oxide nanotubes and nanorods, *Mater. Chem. Phys.* 133 (2012) 605–610.
- [32] W. Yang, Z. Su, Z. Xu, W. Yang, Y. Peng, J. Li, Comparative study of α -, β -, γ - and δ -MnO₂ on toluene oxidation: oxygen vacancies and reaction intermediates, *Appl. Catal. B* 260 (2020), 118150.
- [33] Z. Liu, R. Ma, Y. Ebina, K. Takada, T. Sasaki, Synthesis and delamination of layered manganese oxide nanobelts, *Chem. Mater.* 19 (2007) 6504–6512.
- [34] D. Li, M.H. Nielsen, J.R. Lee, C. Frandsen, J.F. Banfield, J.J. De Yoreo, Direction-specific interactions control crystal growth by oriented attachment, *Science* 336 (2012) 1014–1018.
- [35] G.P. Ojha, B. Pant, A. Muthurasu, S.H. Chae, S.J. Park, T. Kim, H.Y. Kim, Three-dimensionally assembled manganese oxide ultrathin nanowires: prospective electrode material for asymmetric supercapacitors, *Energy* 188 (2019), 116066.
- [36] C. Wang, Y. Hu, C.M. Lieber, S. Sun, Ultrathin Au nanowires and their transport properties, *J. Am. Chem. Soc.* 130 (2008) 8902–8903.
- [37] X. Lu, M.S. Yavuz, H.Y. Tuan, B.A. Korgel, Y. Xia, Ultrathin gold nanowires can be obtained by reducing polymeric strands of oleylamine-AuCl complexes formed via aurophilic interaction, *J. Am. Chem. Soc.* 130 (2008) 8900–8901.
- [38] X. Liang, J.E. Post, B. Lanson, X. Wang, M. Zhu, F. Liu, W. Tan, X. Feng, G. Zhu, X. Zhang, J.J.D. Yoreo, Coupled morphological and structural evolution of δ -MnO₂ to α -MnO₂ through multistage oriented assembly processes: the role of Mn (III), *Environ. Sci. Nano* 7 (2020) 238–249.
- [39] L. Li, P. Zhang, R. Cao, Porous manganese oxides synthesized with natural products at room temperature: a superior humidity-tolerant catalyst for ozone decomposition, *Catal. Sci. Technol.* 10 (2020) 2254–2267.
- [40] S. Mo, Q. Zhang, J. Li, Y. Sun, Q. Ren, S. Zou, Q. Zhang, J. Lu, M. Fu, D. Mo, J. Wu, H. Huang, D. Ye, A Highly efficient mesoporous MnO₂ catalysts for the total

- toluene oxidation: oxygen-vacancy defect engineering and involved intermediates using in situ DRIFTS, *Appl. Catal. B* 264 (2020), 118464.
- [41] K. Qi, J. Xie, H. Hu, D. Han, D. Fang, P. Gong, F. Li, F. He, X. Liu, Facile synthesis of Mn-based nanobelts with high catalytic activity for selective catalytic reduction of nitrogen oxides, *Chem. Eng. J.* 352 (2018) 39–44.
- [42] S. Zhu, H. Zhang, P. Chen, L.H. Nie, C.H. Li, S.K. Li, Self-assembled three-dimensional hierarchical graphene hybrid hydrogels with ultrathin β -MnO₂ nanobelts for high performance supercapacitors, *J. Mater. Chem. A* 3 (2015) 1540–1548.
- [43] S. Rong, T. He, P. Zhang, Self-assembly of MnO₂ nanostructures into high purity three-dimensional framework for high efficiency formaldehyde mineralization, *Appl. Catal. B* 267 (2019), 118375.
- [44] W. Si, Y. Wang, S. Zhao, F. Hu, J. Li, A facile method for in-situ preparation of the MnO₂/LaMnO₃ catalyst for the removal of toluene, *Environ. Sci. Technol.* 50 (2016) 4572–4578.
- [45] S. Rong, P. Zhang, Y. Yang, L. Zhu, J. Wang, F. Liu, MnO₂ framework for instantaneous mineralization of carcinogenic airborne formaldehyde at room temperature, *ACS Catal.* 7 (2017) 1057–1067.
- [46] V.P. Santos, O.S.G.P. Soares, J.J.W. Bakker, M.F.R. Pereira, J.J.M. Órfão, J. Gascon, F. Kapteijn, J.L. Figueiredo, Structural and chemical disorder of cryptomelane promoted by alkali doping: influence on catalytic properties, *J. Catal.* 293 (2012) 165–174.
- [47] H. Sun, X. Yu, X. Yang, X. Ma, M. Lin, C. Shao, Y. Zhao, F. Wang, M. Ge, Au/Rod-like MnO₂ catalyst via thermal decomposition of manganite precursor for the catalytic oxidation of toluene, *Catal. Today* 332 (2019) 153–159.
- [48] X. Yang, X. Yu, M. Lin, X. Ma, M. Ge, Enhancement effect of acid treatment on Mn₂O₃ catalyst for toluene oxidation, *Catal. Today* 327 (2019) 254–261.
- [49] Y. Luo, Y. Zheng, J. Zuo, X. Feng, X. Wang, T. Zhang, K. Zhang, L. Jiang, Insights into the high performance of Mn-Co oxides derived from metal-organic frameworks for total toluene oxidation, *J. Hazard. Mater.* 349 (2018) 119–127.
- [50] L. Zhao, Z. Zhang, Y. Li, X. Leng, T. Zhang, F. Yuan, X. Niu, Y. Zhu, Synthesis of Ce_{0.8}MnO_x hollow microsphere with hierarchical structure and its excellent catalytic performance for toluene combustion, *Appl. Catal. B* 245 (2019) 502–512.
- [51] S. Mo, S. Li, W. Li, J. Li, J. Chen, Y. Chen, Excellent low temperature performance for total benzene oxidation over mesoporous CoMnAl composited oxides from hydrotalcites, *J. Mater. Chem. A* 4 (2016) 8113–8122.
- [52] Y. Yang, J. Jia, Y. Liu, P. Zhang, The effect of tungsten doping on the catalytic activity of α -MnO₂ nanomaterial for ozone decomposition under humid condition, *Appl. Catal. A Gen.* 562 (2018) 132–141.
- [53] S. Gligorovski, R. Strekowski, S. Barbat, D. Vione, Environmental Implications of Hydroxyl Radicals (\bullet OH), *Chem. Rev.* 115 (2015) 13051–13092.
- [54] L.F. Liao, C.F. Lien, J.L. Lin, FTIR study of adsorption and photoreactions of acetic acid on TiO₂, *Phys. Chem. Chem. Phys.* 3 (2001) 3831–3837.
- [55] Y. He, Z. Rui, H. Ji, In situ DRIFTS study on the catalytic oxidation of toluene over V₂O₅/TiO₂ under mild conditions, *Catal. Commun.* 14 (2011) 77–81.
- [56] J. Wang, J. Li, C. Jiang, P. Zhou, P. Zhang, J. Yu, The effect of manganese vacancy in birnessite-type MnO₂ on room-temperature oxidation of formaldehyde in air, *Appl. Catal. B* 204 (2017) 147–155.
- [57] C. Zhang, F. Liu, Y. Zhai, H. Ariga, N. Yi, Y. Liu, K. Asakura, M. Flytzani-Stephanopoulos, H. He, Alkali-metal-promoted Pt/TiO₂ opens a more efficient pathway to formaldehyde oxidation at ambient temperatures, *Angew. Chem. Int. Ed.* 51 (2012) 9628–9632.
- [58] X. Li, P. Zhang, L. Jin, T. Shao, Z. Li, J. Cao, Efficient photocatalytic decomposition of perfluorooctanoic acid by indium oxide and its mechanism, *Environ. Sci. Technol.* 46 (2012) 5528–5534.
- [59] B. Liu, C. Li, G. Zhang, X. Yao, S.S. Chuang, Z. Li, Oxygen vacancy promoting dimethyl carbonate synthesis from CO₂ and methanol over Zr-doped CeO₂ nanorods, *ACS Catal.* 8 (2018) 10446–10456.